

RESEARCH LETTER

10.1002/2016GL069800

Key Points:

- Stress drops of induced earthquakes are on the high end of the normal range (5–80 MPa)
- Stress drops do not vary with depth or distance from the well, and no scaling is observed for M_w 3–4
- Stress drops alone are insufficient in the differentiation of induced and tectonic events

Supporting Information:

- Supporting Information S1
- Table S1

Correspondence to:

F. Clerc,
fiona.clerc@mail.mcgill.ca

Citation:

Clerc, F., R. M. Harrington, Y. Liu, and Y. J. Gu (2016), Stress drop estimates and hypocenter relocations of induced seismicity near Crooked Lake, Alberta, *Geophys. Res. Lett.*, 43, 6942–6951, doi:10.1002/2016GL069800.

Received 6 FEB 2016

Accepted 17 JUN 2016

Accepted article online 23 JUN 2016

Published online 14 JUL 2016

Corrected 4 AUG 2016

This article was corrected on 4 AUG 2016. See the end of the full text for details.

Stress drop estimates and hypocenter relocations of induced seismicity near Crooked Lake, Alberta

Fiona Clerc¹, Rebecca M. Harrington¹, Yajing Liu¹, and Yu Jeffrey Gu²

¹Department of Earth and Planetary Sciences, McGill University, Montreal, Quebec, Canada, ²Department of Physics, University of Alberta, Edmonton, Alberta, Canada

Abstract We use a sequence of induced earthquakes near Crooked Lake, Alberta, to investigate the physical differences between induced and tectonic earthquakes. Starting with the Natural Resources Canada earthquake catalogue, we use a spectral ratio method to calculate the static stress drops of a group of relocated earthquakes ranging from December 2013 to June 2015. We find that stress drops fall within the high side of the typical reported range of tectonic events and show no correlation with earthquake magnitude, depth, or distance from the well. The stress drops appear roughly constant for events with M_w 3 to 4. Relocated hypocenters cluster both spatially and temporally around corresponding injection wells and appear to migrate deeper with increasing time from injection. Fine-scale lineations apparent in relocated hypocenters could indicate the presence and orientation of fault planes, consistent with the published focal mechanism solutions of M 4+ events in the area.

1. Introduction

Human-induced earthquakes resulting from poroelastic stress changes due to subsurface fluid injection pose a potential risk to surrounding populations [e.g., *Raleigh et al.*, 1976; *BC Oil and Gas Commission*, 2012, 2014; *Ellsworth*, 2013; *McGarr*, 2014; *Eaton and Mahani*, 2015; *Schultz et al.*, 2015b]. Whether nucleated by wastewater disposal, enhanced geothermal stimulation, or hydraulic fracturing, induced earthquakes can have large enough magnitudes to damage nearby infrastructure [*Keranen et al.*, 2013, 2014]. A fundamental step in developing a magnitude-predictable relationship between operational parameters and induced events is to identify any physical differences or similarities between induced and (naturally occurring) tectonic earthquakes; the key lies in their source parameters.

A number of studies have investigated the focal mechanisms of induced events in attempts to explore distinguishing characteristics between induced and tectonic earthquakes. For example, *Eaton and Mahani* [2015] observe variability between fault plane orientations of suspected hydraulic fracturing induced events from the Crooked Lake and Rocky Mountain House clusters in the Western Canada Sedimentary Basin (WCSB), suggesting that the fault plane orientations of induced events can indicate local deviations from the regional stress field. In a full moment tensor inversion study, *Zhang et al.* [2016] found that eight M 3.2–4.4 induced earthquakes in the WCSB generally have higher nondouble-couple components than a tectonic earthquake in the same region, which may result from the presence of multiple intersecting fractures, dilatant jogs, or nonplanar preexisting faults. In particular, a M_w 3.9 event (M_w 4.6 in the Natural Resources Canada (NRCAN) catalogue) on 13 June 2015, near Fox Creek, exhibits a strong strike-slip focal mechanism that differs considerably from the thrust or dip-slip events found along the foothills [*Wang et al.*, 2016]. However, in some cases, induced and natural earthquakes have similar focal mechanisms, most likely because these induced events occur on reactivated faults consistent with the regional stress field orientation. For example, the focal mechanism solutions and hypocenter depths of hydraulic fracturing and wastewater disposal induced events in the Poland Township and Youngstown, Ohio, sequences [*Skoumal et al.*, 2015] suggest reactivation along existing fault orientations, consistent with the regional stress field. Similarly, a moment tensor inversion from *Schultz et al.* [2015b] links the Cardston, Alberta, earthquake swarm to an existing basement fault, reactivated by the increase in pore pressure due to hydraulic fracturing.

Another earthquake source parameter that may potentially be used to discriminate between induced and natural events is the static stress drop. Stress drop studies of natural events suggest that values typically range

between 0.1 to 100 MPa with constant stress drop scaling over a large range of magnitudes [e.g., *Abercrombie, 1995; Ide and Beroza, 2001; Abercrombie and Rice, 2005*]. In her development of ground motion prediction equations for induced events, *Atkinson [2015]* notes the importance of stress drops in determining the amplitude of ground motion and degree of seismic hazard. By investigating the b value of seismicity surrounding Fox Creek, *Atkinson et al. [2015]* conclude that the seismic hazard of induced events is more significant due to their shallow hypocentral depths, while making the key assumption that stress drops of induced events are similar to those of natural events. Through a comparison of intensity distribution data, *Hough [2014]* suggests that the stress drops of induced earthquakes in central and eastern U.S. are lower than tectonic events in the same region by a factor of 2 to 10. However, a recent study by *Zhang et al. [2016]* analyzes the individual spectral fits of $M 4+$ potentially induced earthquakes in the WCSB and find consistent static stress drops ranging from 2 to 90 MPa. These values are typical of tectonic events, although their large uncertainties can be attributed to the spread of estimated corner frequencies at different stations for the individual earthquakes.

In this study, we aim to precisely estimate the static stress drops of potentially induced earthquakes using the spectral ratio and empirical Green's function (EGF) method. We focus our analysis on the Crooked Lake earthquake sequence between December 2013 and June 2015, using waveform data from a number of regional networks. Our EGF analysis results in high stress drops in ranging from 11 to 93 MPa that appear roughly scale invariant over the range of M_w 3 to 4. There is no clear dependence of stress drops on event depths or distances from the well. Finally, double-difference hypocenter relocations suggest the migration of the event depths with time, which may reflect the spatial-temporal variation of poroelastic stress change due to injection.

2. Data and Methods

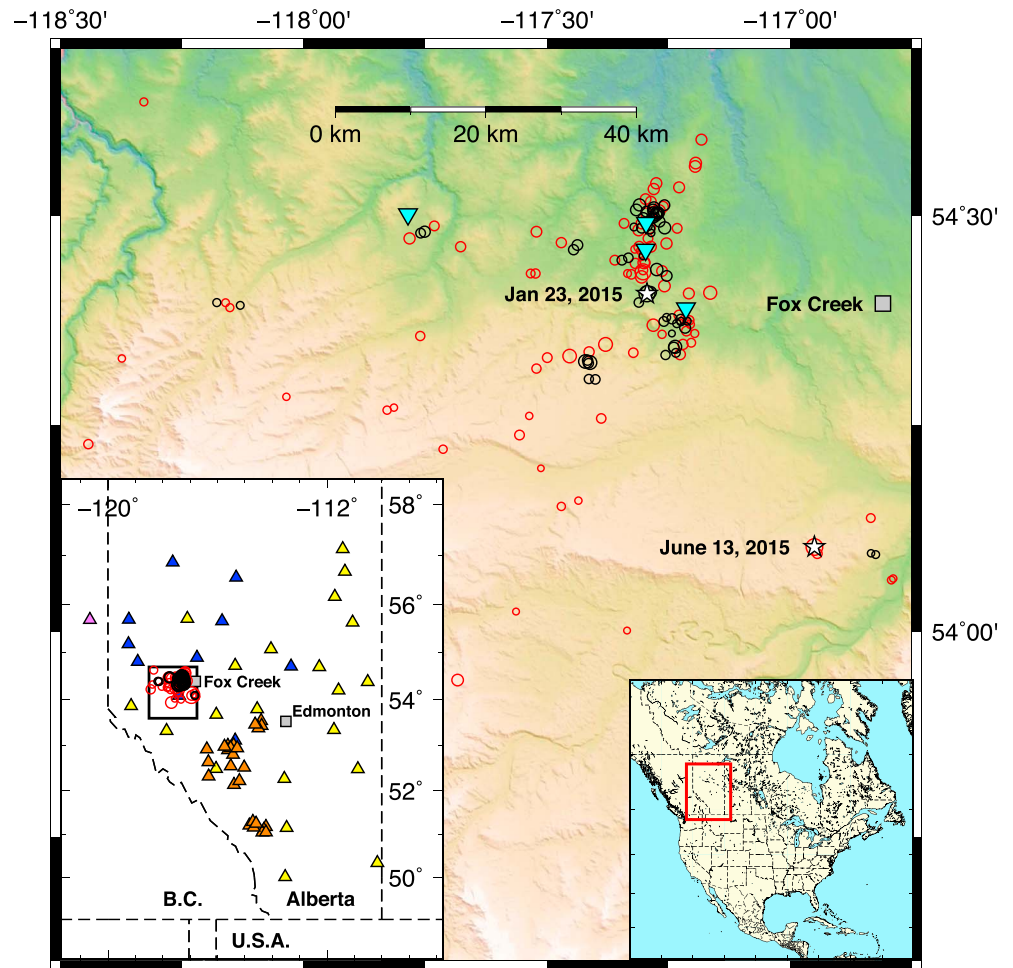
Previously a region of seismic inactivity, the area near Fox Creek, Alberta, has drawn attention following the onset of events likely induced by hydraulic fracturing operations. In the meantime, seismic station coverage in western Canada has increased significantly in recent years [e.g., *Gu et al., 2011; Novakovic and Atkinson, 2015*], where additional stations were deployed for the purposes of monitoring induced earthquakes. *Schultz et al. [2015a]* establish a temporal correlation of $>99.99\%$ between the timing of these operations and the induced events from 2013 to 2014, further dividing the sequence into temporal clusters corresponding spatially to the positions of multiple injection sites. Although the events of 2015 have not been definitively linked to hydraulic fracturing operations, their proximity to the wells and the scarcity of previous natural seismicity suggest these operations as the most plausible source. Of particular interest is the M_L 4.4 event of 23 January 2015 and the M_w 4.6 event of 13 June 2015, which constitute the largest events in the area as of 2015 [*Earthquakes Canada, 2015*].

We begin with a list of 82 events (M 1.8 to M 4.6) from the NRCan Earthquake Catalogue, hereafter NRCan, from December 2013 to June 2015. We obtain waveform data from the TD, RAVEN [*Schultz and Stern, 2015*], CRANE [*Gu et al., 2011*], and CN networks (Figure 1), where the majority of the stations have a sampling rate of 100 sps while others are sampled at a rate of 40 sps. After removing instrument response and filtering from 0.5 Hz to the Nyquist frequency, we cut the raw data into 4 s windows beginning 0.5 s before the respective P and S wave arrivals. The analysis has also been performed using time windows of 2 s and 6 s, but a time window of 4 s was chosen as it resolves the spectra at lower frequencies, while still excluding subsequent phase arrivals.

For both stress drop calculation and event relocation, we use an updated 1-D velocity model at the PER station of the CRANE network [*Chen et al., 2015*]. At depths of 2–5 km, the P wave velocity is 5.70 km/s and the S wave velocity is 3.22 km/s. At shallower depths this velocity model is also consistent with the *Eaton and Mahani [2015]* model taken from borehole data.

2.1. Hypocenter Relocations

In order to better constrain the association of the earthquakes in the Crooked Lake sequence to individual wells, we exploit the increased coverage to refine the catalogue locations in our data set by calculating double-difference hypocenter relocations using hypoDD [*Waldhauser and Ellsworth, 2000, 2002*]. We use 27 stations within 250 km of the NRCan reported epicentral locations to determine catalogue and cross-correlation traveltimes differences and estimate the relocation uncertainty using 1000 trials of a bootstrap random replacement of traveltimes residuals following *Waldhauser and Ellsworth [2000]*. Using the 1-D velocity model of *Chen et al. [2015]*, we perform the relocation calculation using a total of 3164 and 4680



▲ CRANE	▲ RAVEN	▲ TD	▲ CN
○ HypoDD relocations (this study)	○ NRCan locations		
• M 1	○ M 2	○ M 3	○ M 4
▼ Hydraulic fracturing wells	□ Municipalities		

Figure 1. Map showing event locations; station coverage of the study area (Crooked Lake sequence, Alberta) is shown in the inset. Seismic stations are marked by triangles. Circles indicate both the NRCan catalogue locations and double-difference relocations. Stars denote the magnitude 4.4 and 4.6 events of 23 January 2015 and 13 June 2015, respectively.

catalogue and cross-correlation traveltimes differences, respectively. Cross-correlation traveltimes differences were calculated by requiring a cross-correlation coefficient of 0.7 or greater between event waveforms.

2.2. Stress Drop Estimation

We first use the spectral amplitude of single events to determine corner frequencies and long-period amplitudes (section 2.2.1) and subsequently calculate earthquake moments. The corner frequency estimates are then refined using a spectral ratio method (section 2.2.2). Finally, static stress drops are calculated by combining the moment and corner frequency estimates from the above two steps.

2.2.1. Amplitude Spectra of Single Events

In order to determine the moments of individual events, we convert our waveforms into the frequency domain and calculate the spectral amplitude using Thomson’s multitaper method [Thomson, 1982]. We fit the spectrum to the Brune [1970, 1971] model shown in equation (1), where Ω_0 is the long-period spectral amplitude,

f is the spectral frequency, f_c is the spectral corner frequency, n is the high-frequency falloff rate, γ is a constant that is commonly set to 2 [Boatwright, 1980], Q is the quality factor, and t is the travelttime,

$$\Omega(f) = \frac{\Omega_0 e^{-\frac{\pi ft}{Q}}}{\left[1 + \left(\frac{f}{f_c}\right)^{\gamma n}\right]^{\frac{1}{\gamma}}}. \quad (1)$$

As in *Abercrombie* [1995], we alternate the free parameters in four different models and use the trust region reflective least squares algorithm in MATLAB, finding that Ω_0 does not vary considerably from one model to another. We use the residuals to estimate 95% confidence intervals and conclude that the model best approximates the data when we allow n , f_c , and Ω_0 to vary but constrain $Q = 1000$. The constant quality factor has a negligible effect on the low-frequency limit of the amplitude spectrum. Robust Ω_0 estimates are thus obtained, from which we can calculate moments as follows:

$$M_0 = \frac{4\pi\rho c^3 R \Omega_0}{U_{\phi\theta}}, \quad (2)$$

where density, $\rho = 2700 \text{ kg/m}^3$, the P or S wave speed, c , is from our velocity model, the distance R from the event is determined using the hypocenter relocations (or catalogue locations where relocations were discarded), and the mean radiation pattern, $U_{\phi\theta}$, of 0.52 for P waves and 0.63 for S waves [Aki and Richards, 2002]. The resulting moment magnitudes M_w [Hanks and Kanamori, 1979] are compared to the local magnitudes M_L provided by the NRCan catalogue in Figure S1 in the supporting information. The two magnitude measurements correlate along a line of slope of 1 with little scatter; however, our calculated M_w values for larger events are slightly lower than the corresponding catalogue M_L values (see supporting information). We calculate the weighted means of our moment magnitudes across multiple stations for a given event and use the propagated confidence intervals from the least squares fit as our error estimate.

2.2.2. Spectral Ratios and the EGF Method

Once we have determined the precise relocations and moments for each of the catalogued events, we then use a spectral ratio method to constrain the corner frequencies precisely. For a given earthquake, its ground motion (m) can be expressed as a convolution of source (s_0), site (i), and path effects (p) using the empirical Green's function.

$$m(t) = s_0(t) * p(t) * i(t). \quad (3)$$

Using carefully selected colocated event pairs, the spectral ratio approach allows us to remove travel path, site, and receiver effects (and consequently attenuation effects) in order to better constrain the source term and subsequently the corner frequencies [e.g., Ide et al., 2003; Abercrombie and Rice, 2005]. In the frequency domain, the ratio of the ground motion of the larger event (main event) to that of the smaller one (EGF event) would theoretically form two plateaus, which transition at two corner frequencies. The lower corner frequency (f_{c1}) corresponds to the larger event and the higher one (f_{c2}) to the smaller event. Events that rupture the same patch of a fault will have similar waveforms and high cross-correlation coefficients. In order to keep only event pairs that are colocated, we discard those with a cross-correlation coefficient lower than 0.7. We impose a minimum magnitude difference of 0.3 between the two events in order to observe a discernible spectral ratio with a resolvable difference in corner frequencies. If stress drop values between events in a colocated pair are similar, one typically requires a larger magnitude difference. However, stress drops can vary over an order of magnitude for a given moment, and source dimensions may vary accordingly. To account for such differences in stress drop and retain the highest number of available event pairs, we therefore use a small minimum magnitude difference and discard event pairs without a resolvable difference in corner frequencies (and therefore similar source dimensions).

The signal-to-noise ratio (SNR) is evaluated at intervals of 1 Hz, and only the data from those intervals with a $\text{SNR} > 3$ are used. A minimum bandwidth of 20 Hz is required over which the spectral ratio is fitted using *Brune's* [1970] model. In cases where the lower frequency plateau is partially missing but the data are otherwise clean, we extend the low-frequency end of the spectrum using the mean of the first four points, allowing the least squares algorithm to converge on a reasonable corner frequency estimate. In cases where the corner frequency of the smaller event converges on the Nyquist frequency and had to be categorized

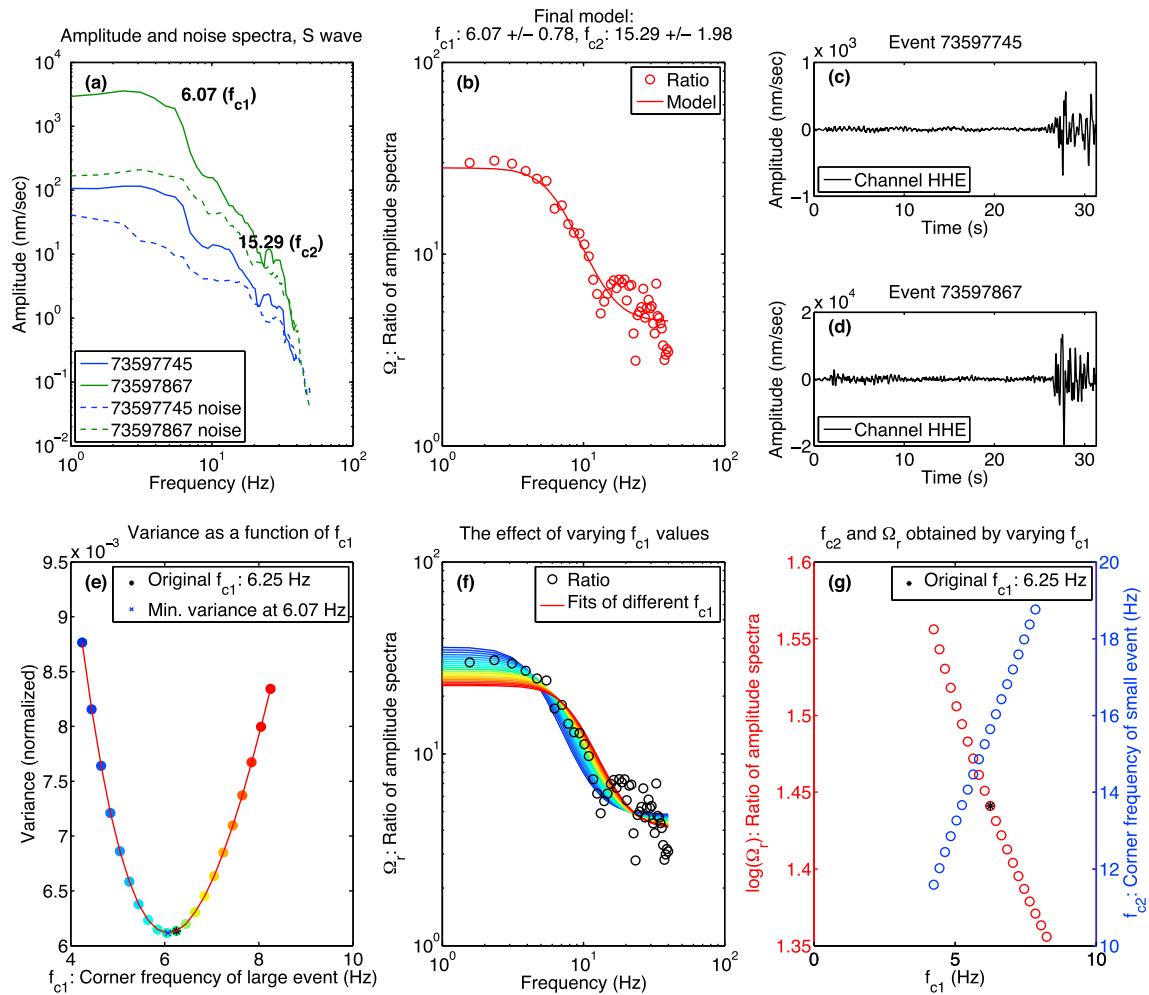


Figure 2. The spectral ratio fits for a representative event pair. (a) The spectral amplitude and noise spectra of each event. (b) The spectral ratio and the model fit with the final corner frequency estimates. (c and d) The waveforms in the time domain (note the similarity). (e) The variance (chi-square misfit) of incremented values of f_{c1} , each value is represented by a different color. (f) The corresponding fits to the data at different f_{c1} increments. The same color convention is used for the fits shown in this panel and for the variance in Figure 2e. The model is evaluated at each f_{c1} increment, and (g) the resulting Ω_r , r , and f_{c2} values are plotted against f_{c1} .

as a minimum estimate, we retain only the fits of the larger event corner frequency (reflecting the bandwidth limitations of the data, as addressed in *Abercrombie* [2015]).

In order to determine robust fits and quantify uncertainties, following an initial least squares fit, we take the corner frequency of the larger event, f_{c1} , and increment it by 0.2 Hz to 2 Hz before and after the original value. We then fit the data again, keeping f_{c1} fixed at each increment, as in *Viegas et al.* [2010], *Kane et al.* [2011], and *Abercrombie* [1995]. We calculate and plot the normalized variance, discarding pairs with variances that do not form a parabola. We take the f_{c1} of minimum variance, calculated using chi-square misfit values, as our final f_{c1} estimate, and compute a confidence interval by taking the width of the parabola where there is a 5% increase in variance, as in *Viegas et al.* [2010]. Similarly, the model was evaluated at different values of f_{c2} , and a 5% confidence interval from the variance parabola was used to estimate the error on f_{c2} . Figure 2 shows a representative example of a robust spectral ratio fit. We visually inspect all spectral ratio fits and discard unreasonable ones, such as in the absence of well-defined plateaus. We take the weighted mean of the corner frequencies of each event using the confidence interval from the variance parabolas as the error estimate.

Using the moments from the single spectrum fits and corner frequencies from the spectral ratio fits, we calculate the stress drop of each event using the expression for a penny-shaped crack [*Eshelby*, 1957],

$$\Delta\sigma = \frac{7}{16} \frac{M_0}{r^3}. \tag{4}$$

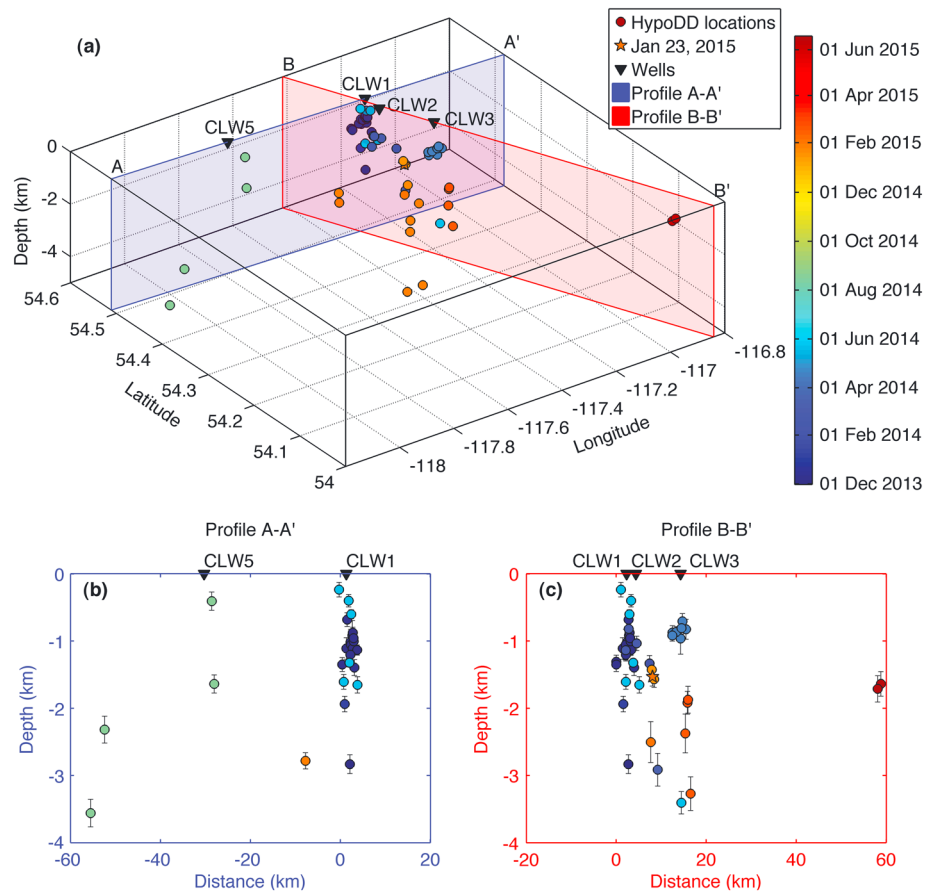


Figure 3. (a) Three-dimensional plot of hypocenter relocations. Colors correspond to time, and black triangles show the location of injection wells [Schultz et al., 2015a]. Vertical planes pass through the wells; seismicity is projected onto the planes (b) A-A' and (c) B-B', illustrating the depth distribution onto these profiles. Injection occurred December 2013 and May 2014 for CLW1, February 2014 for CLW2, and March 2014 for CLW3 [Schultz et al., 2015a].

The source radius, r , is obtained from the Madariaga [1976] circular source model,

$$r = \frac{k\beta}{f_c} \tag{5}$$

where β is the shear wave velocity (we use 3220 m/s [Chen et al., 2015]) and k is 0.315 for P waves and 0.21 for S waves.

3. Results

3.1. Hypocenter Relocations

In total, we relocate 58 of the original 82 catalogued events (Figure 3). Hypocenter depths are shallow and do not exceed 5 km, which justifies the choice of the velocity values mentioned in section 2. Horizontal errors are on the order of 0.3 km, while depths are typically less well constrained, with errors on the order of 2 km. In some cases the relocation did not converge on a single depth, and so the NRCan catalogue location was used in the stress drop calculations. Event relocations are grouped into clusters, whose locations coincide with the positions of the respective injection wells (Figure 3).

3.2. Stress Drop Values

We plot the corner frequency against moment (Figure 4) and note that the general trend of values follows the theoretically predicted inverse relation between the two parameters for constant stress drop scaling, $M_0 \propto f_c^{-3}$. The slope of the line that best fits the data is -0.115 for all data points and -0.387 for moments higher than 5×10^{13} N m (above which there are no more poorly constrained f_c values). When the stress drops are plotted against moment, there is much scatter and no discernible trend at magnitudes lower than 5×10^{13} N m.

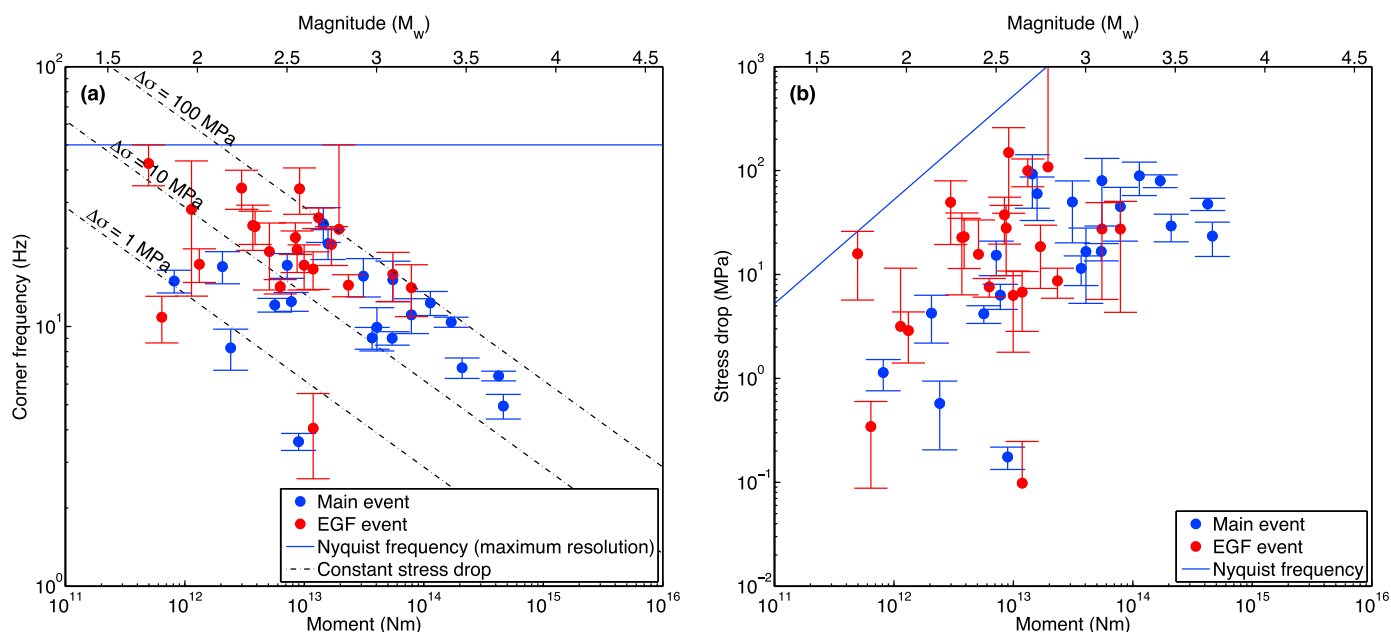


Figure 4. (a) Station-averaged corner frequency versus station-averaged moment values. Blue versus red colors indicate whether the event is the larger (main) or smaller (EGF) event of the spectral ratio pair. The blue line marks the Nyquist frequency and upper limit of the bandwidth of observation. Black dashed lines mark lines of constant stress drop of *P* waves. (b) Station-averaged stress drops versus station-averaged moment values.

In general, stress drop estimates for all the events in this study range from 0.1 to 149 MPa, while at greater magnitudes ($M_0 > 5 \times 10^{13}$ N m) we observe constant stress drops that range from 11 to 93 MPa. Errors on the stress drops are on the order of 1 to 5 MPa, a reflection of corner frequency errors ranging from 0.1 to 1 Hz. A comparison of stress drop estimates with depths obtained from the relocations, as well as with distance from the corresponding injection well, shows weak correlation with each parameter (Figures S2 and S3), as correlation coefficients are 0.44 and 0.14, respectively.

4. Discussion

4.1. Relocations

The events forming a cluster around each injection well correspond to the same time period (Figure 3). By comparing our relocations to the injection schedule from *Schultz et al.* [2015a], we qualitatively reach the same conclusion of high temporal correlation between injection and seismicity for the 2014 events. The location of events from 2015 in relation to their injection wells could not be investigated as the injection data are not publicly accessible at the time of this study. Our relocations are generally shallower than those calculated by *Schultz et al.* [2015a], perhaps because their velocity model is based on well logging information while ours comes from a recent regional velocity inversion study [*Chen et al.*, 2015]. Given that hydraulic fracturing occurs at a depth of 3.4–3.5 km, the shallower hypocenters obtained here are suggestive of greater uncertainties associated with our relocations (≈ 2 km vertical uncertainty).

Figure 3 indicates that for a given cluster associated with an individual well, events get progressively deeper with time, presumably due to the diffusion of fluid from the injection site. The fine-scale lineations within each cluster may result from earthquakes occurring on preexisting fault planes. *Schultz et al.* [2016] find high spatial correlation between fossil reef structures and seismicity distribution in the WCSB, suggesting the existence of near-basement faults. Similarities between event distribution and focal mechanism orientations would imply the reactivation of preexisting faults by poroelastic stress changes.

4.2. Stress Drops

The calculated stress drops, 0.1 to 149 MPa, fall within the typical range observed for tectonic earthquakes, albeit on the high end. These higher values are inconsistent with the prediction that induced seismic events have lower stress drops than tectonic earthquakes of the same region [*Hough*, 2014]. Spectral ratio methods

commonly correct for nonsource-related effects such as attenuation, the presence of which could otherwise lead to underestimated corner frequency and stress drops [e.g., *Ide et al.*, 2003]. As this study is one of the first to estimate stress drops of induced events using spectral ratio methods, our results suggest that a similar approach to the removal of attenuation effects could yield equally high stress drop values in other induced sequences.

Although high, our stress drop values are not anomalous, even for smaller earthquakes; as seen in Figure 8 of *Kwiatek et al.* [2011], a compilation of stress drop values from studies of both induced and natural earthquakes shows values ranging between 10 and 100 MPa over the entire magnitude range ($-4 < M < 4$). Relatively high stress drops seem to be characteristic of the WCSB. For example, *Zhang et al.* [2016] report a stress drop range of 2 to 90 MPa for events of $M_w > 3.5$, similar to our range of 11 to 93 MPa. Our stress drop estimates for the 13 June 2015 event agree with that of *Wang et al.* [2016], calculated by fitting the Brune model to the pseudoacceleration spectral amplitudes; their estimate is 6 MPa, consistent within the error range of our calculations ($5.45 \text{ MPa} \pm 1.28 \text{ MPa}$). Quantifying the reasons for enhanced stress drops in the WCSB will be an important subject for future studies of induced earthquake source processes.

The scatter of stress drops from events with seismic moments below $5 \times 10^{13} \text{ N m}$ does not permit us to draw any robust conclusion regarding stress drop scaling for smaller events (Figure 4). The unconstrained stress drop values for events with high corner frequencies are artifacts of the lower SNR of events with smaller amplitudes. Furthermore, the SNR becomes even poorer at higher frequencies. The corner frequencies of the EGF events of the spectral ratio pairs (the red data points in Figure 4) have significantly larger uncertainties, due in part to the minimization of f_{c1} errors at the expense of the f_{c2} estimates (see Figure 2g). Bandwidth limitations introduce further bias [*Ide and Beroza*, 2001], as we could not calculate corner frequencies above 50 Hz. The underestimation of corner frequencies at smaller magnitudes lowers stress drop estimates for smaller events.

Stress drops from events of moment greater than $5 \times 10^{13} \text{ N m}$ show no visible dependency on magnitude. The slope of the line approximating the relation between the corner frequency and moment is very close to the theoretically predicted value for constant stress drop scaling. We suspect that the events of the Crooked Lake Sequence may be scale invariant at higher magnitudes, though we are limited by our observations, and do not attempt to make robust claims about stress drop scaling.

Concerning the variation of the stress drop estimates with distance from the well, we observe no correlation between stress drops and depth or distance from the well (Figures S2 and S3). We note that the lack of depth or distance dependence contrasts the findings of *Goertz-Allmann et al.* [2011]. However, they considered primarily events within 300 m of the injection point, while the majority of our events are recorded at greater distances. Additionally, differences in lithology must be taken into account; the Basel geothermal site of the *Goertz-Allmann et al.* [2011] study is based on crystalline rock, as opposed to the tight shale found near Fox Creek.

In summary, the stress drop estimates obtained in this study do not conclusively differentiate these events from tectonic earthquakes. This is especially true considering the error inherent in stress drop calculations, due in part to its dependence on the corner frequency cubed. The relocation results are more indicative of induced seismicity than the stress drop estimates.

5. Conclusion

Following the application of the spectral ratio method to robustly estimate spectral corner frequency values for a series of induced earthquakes, we find that stress drop estimates are normal but higher than expected, consistent with other regional studies, and range from 11 to 93 MPa within the M_w 3 to 4 range. The stress drops are also scale invariant within this range, while at lower magnitudes noise and bandwidth limitations introduce too much scatter to make definitive conclusions regarding scaling relations. Stress drop estimates show no dependence on the depth or distance from the injection well. Our findings imply that neither stress drop amplitude nor scaling are reliable metrics in distinguishing induced and tectonic earthquakes, as stress drop range may be greatly affected by the regional setting. On the other hand, the double-difference relocations, which group these events spatially into distinct clusters near known injection wells, may be a more reliable indicator of induced seismicity than stress drop estimates.

Acknowledgments

Waveform data from the TD, RAVEN, and CN networks were obtained through the Incorporated Research Institutions for Seismology (IRIS), available online. Data were also obtained from the CRANE network, owned and operated by the University of Alberta. The map (Figure 1) was created using the Generic Mapping Tools program [Wessel et al., 2013], and the topography data were obtained from Jarvis et al. [2008]. We thank Ruijia Wang for her comments which helped improve the quality of the manuscript. Support for this work was provided by the Natural Sciences and Engineering Research Council of Canada and by the Fonds de recherche du Québec—Nature et technologies.

References

- Abercrombie, R. E. (1995), Earthquake source scaling relationships from -1 to $5 M_L$ using seismograms recorded at 2.5-km depth, *J. Geophys. Res.*, *100*(B12), 24,015–24,036.
- Abercrombie, R. E. (2015), Investigating uncertainties in empirical Green's function analysis of earthquake source parameters, *J. Geophys. Res. Solid Earth*, *120*(6), 4263–4277, doi:10.1002/2015JB011984.
- Abercrombie, R. E., and J. R. Rice (2005), Can observations of earthquake scaling constrain slip weakening?, *Geophys. J. Int.*, *162*(2), 406–424, doi:10.1111/j.1365-246X.2005.02579.x.
- Aki, K., and P. G. Richards (2002), *Quantitative Seismology*, 2nd ed., vol. 704, Univ. Science Books, Sausalito.
- Atkinson, G. M. (2015), Ground-motion prediction equation for small-to-moderate events at short hypocentral distances, with application to induced-seismicity hazards, *Bull. Seismol. Soc. Am.*, *105*(2A), 981–992, doi:10.1785/0120140142.
- Atkinson, G. M., H. Ghofrani, and K. Assatourians (2015), Impact of induced seismicity on the evaluation of seismic hazard: Some preliminary considerations, *Seismol. Res. Lett.*, *86*(3), 1009–1021, doi:10.1785/0220140204.
- BC Oil and Gas Commission (2012), Investigation of observed seismicity in the Horn River Basin. Oil and Gas Commission, Victoria, BC. [Available at <https://www.bcogc.ca/investigation-observed-seismicity-horn-river-basin>.]
- BC Oil and Gas Commission (2014), Investigation of observed seismicity in the Montney Trend. Oil and Gas Commission, Victoria, BC. [Available at <http://www.bcogc.ca/sites/default/files/documentation/technical-reports/investigation-observed-seismicity-montney-trend.pdf>.]
- Boatwright, J. (1980), A spectral theory for circular seismic sources: Simple estimates of source dimension, dynamic stress drop, and radiated seismic energy, *Bull. Seismol. Soc. Am.*, *70*(1), 1–27.
- Brune, J. N. (1970), Tectonic stress and the spectra of seismic shear waves from earthquakes, *J. Geophys. Res.*, *75*(26), 4997–5009.
- Brune, J. N. (1971), Seismic sources, fault plane studies and tectonics, *Eos Trans. AGU*, *52*(5), 178–187, doi:10.1029/EO0521005pIU178.
- Chen, Y., Y. J. Gu, R. M. H. Dokht, and M. D. Sacchi (2015), Crustal imprints of Precambrian orogenesis in western Laurentia, *J. Geophys. Res.*, *120*, 6993–7012, doi:10.1029/2014JB011353.
- Earthquakes Canada (2015), GSC, Earthquake Search (On-line Bulletin). Natural Resources Canada. [Available at <http://earthquakescanada.nrcan.gc.ca/stndon/NEDB-BNDS/bull-eng.php>.]
- Eaton, D. W., and A. B. Mahani (2015), Focal mechanisms of some inferred induced earthquakes in Alberta, Canada, *Seismol. Res. Lett.*, *86*(4), 1078–1085, doi:10.1785/0220150066.
- Ellsworth, W. L. (2013), Injection-induced earthquakes, *Science*, *341*(6142), doi:10.1126/science.1225942.
- Eshelby, J. D. (1957), The determination of the elastic field of an ellipsoidal inclusion, and related problems, *Proc. R. Soc. London, Ser. A*, *241*, 376–396, doi:10.1098/rspa.1957.0133.
- Goertz-Allmann, B. P., A. Goertz, and S. Wiemer (2011), Stress drop variations of induced earthquakes at the Basel geothermal site, *Geophys. Res. Lett.*, *38*(9), L09308, doi:10.1029/2011GL047498.
- Gu, Y. J., A. Okeler, L. Shen, and S. Contenti (2011), The Canadian Rockies and Alberta network (CRANE): New constraints on the Rockies and western Canada sedimentary basin, *Seismol. Res. Lett.*, *82*(4), 575–588, doi:10.1785/gssrl.82.4.575.
- Hanks, T. C., and H. Kanamori (1979), A moment magnitude scale, *J. Geophys. Res.*, *84*(B5), 2348–2350, doi:10.1029/JB084iB05p02348.
- Hough, S. E. (2014), Shaking from injection-induced earthquakes in the central and eastern United States, *Bull. Seismol. Soc. Am.*, *104*(5), 2619–2626, doi:10.1785/0120140099.
- Ide, S., and G. C. Beroza (2001), Does apparent stress vary with earthquake size?, *Geophys. Res. Lett.*, *28*(17), 3349–3352, doi:10.1029/2001GL013106.
- Ide, S., G. C. Beroza, S. G. Prejean, and W. L. Ellsworth (2003), Apparent break in earthquake scaling due to path and site effects on deep borehole recordings, *J. Geophys. Res.*, *108*(B5), 2271, doi:10.1029/2001JB001617.
- Jarvis, A., H. Reuter, A. Nelson, and E. Guevara (2008), Hole-filled seamless SRTM data V4. International Centre for Tropical Agriculture (CIAT). [Available at <http://srtm.csi.cgiar.org>.]
- Kane, D. L., G. A. Prieto, F. L. Vernon, and P. M. Shearer (2011), Quantifying seismic source parameter uncertainties, *Bull. Seismol. Soc. Am.*, *101*(2), 535–543, doi:10.1785/0120100166.
- Keranen, K. M., H. M. Savage, G. A. Abers, and E. S. Cochran (2013), Potentially induced earthquakes in Oklahoma, USA: Links between wastewater injection and the 2011 M_w 5.7 earthquake sequence, *Geology*, *41*(6), 699–702, doi:10.1130/G34045.1.
- Keranen, K. M., M. Weingarten, G. Abers, B. A. Bekins, and S. Ge (2014), Sharp increase in central Oklahoma seismicity since 2008 induced by massive wastewater injection, *Science*, *345*(6195), 448–451, doi:10.1126/science.1255802.
- Kwiatek, G. et al. (2011), Source parameters of picoseismicity recorded at Mponeng deep gold mine, South Africa: Implications for scaling relations, *Bull. Seismol. Soc. Am.*, *101*(6), 2592–2608, doi:10.1785/0120110094.
- Madariaga, R. (1976), Dynamics of an expanding circular fault, *Bull. Seismol. Soc. Am.*, *66*(3), 639–666.
- McGarr, A. (2014), Maximum magnitude earthquakes induced by fluid injection, *J. Geophys. Res. Solid Earth*, *119*(2), 1008–1019, doi:10.1002/2013JB010597.
- Novakovic, M., and G. M. Atkinson (2015), Preliminary evaluation of ground motions from earthquakes in Alberta, *Seismol. Res. Lett.*, *86*(4), 1086–1095, doi:10.1785/0220150059.
- Raleigh, C., J. Healy, and J. Bredehoeft (1976), An experiment in earthquake control at Rangely, Colorado, *Science*, *191*(4233), 1230–1237, doi:10.1126/science.191.4233.1230.
- Schultz, R., and V. Stern (2015), The Regional Alberta Observatory for Earthquake Studies Network (RAVEN), *CSEG Recorder*, *40*(8), 34–37.
- Schultz, R., V. Stern, M. Novakovic, G. Atkinson, and Y. J. Gu (2015a), Hydraulic fracturing and the Crooked Lake Sequences: Insights gleaned from regional seismic networks, *Geophys. Res. Lett.*, *42*(8), 2750–2758, doi:10.1002/2015GL063455.
- Schultz, R., S. Mei, D. Paná, V. Stern, Y. J. Gu, A. Kim, and D. Eaton (2015b), The Cardston earthquake swarm and hydraulic fracturing of the Exshaw Formation (Alberta Bakken Play), *Bull. Seismol. Soc. Am.*, *105*(6), 2871–2884, doi:10.1785/0120150131.
- Schultz, R., H. Corlett, K. Haug, K. Kocon, K. MacCormack, V. Stern, and T. Shipman (2016), Linking fossil reefs with earthquakes: Geologic insight to where induced seismicity occurs in Alberta, *Geophys. Res. Lett.*, *43*, 2534–2542, doi:10.1002/2015GL067514.
- Skoumal, R. J., M. R. Brudzinski, and B. S. Currie (2015), Earthquakes induced by hydraulic fracturing in Poland Township, Ohio, *Bull. Seismol. Soc. Am.*, *105*(1), 189–197, doi:10.1785/0120140168.
- Thomson, D. J. (1982), Spectrum estimation and harmonic analysis, *Proc. IEEE*, *70*(9), 1055–1096, doi:10.1109/PROC.1982.12433.
- Viegas, G., R. E. Abercrombie, and W.-Y. Kim (2010), The 2002 M_5 Sable Forks, NY, earthquake sequence: Source scaling relationships and energy budget, *J. Geophys. Res.*, *115*, B07310, doi:10.1029/2009JB006799.
- Waldhauser, F., and W. L. Ellsworth (2000), A double-difference earthquake location algorithm: Method and application to the northern Hayward fault, California, *Bull. Seismol. Soc. Am.*, *90*(6), 1353–1368, doi:10.1785/0120000006.

- Waldhauser, F., and W. L. Ellsworth (2002), Fault structure and mechanics of the Hayward fault, California, from double-difference earthquake locations, *J. of Geophys. Res.*, *107*(B3), 2054, doi:10.1029/2000JB000084.
- Wang, R., Y. J. Gu, R. Schultz, A. Kim, and G. Atkinson (2016), Source analysis of a potential hydraulic fracturing induced earthquake near Fox Creek, Alberta, *Geophys. Res. Lett.*, *43*, 564–573, doi:10.1002/2015GL066917.
- Wessel, P., W. H. Smith, R. Scharroo, J. Luis, and F. Wobbe (2013), Generic Mapping Tools: Improved version released, *Eos Trans. AGU*, *94*(45), 409–410, doi:10.1029/98EO00426.
- Zhang, H., D. Eaton, G. Li, Y. Liu, and R. M. Harrington (2016), Discriminating induced seismicity from natural earthquakes using moment tensors and source spectra, *J. Geophys. Res. Solid Earth*, *121*, 972–993, doi:10.1002/2015JB012603.

Erratum

The originally published version of this article contained typographical errors. The errors have since been corrected and this version may be considered the authoritative version of record. In figure 2 caption, “(f) The corresponding fits to the data at different f_{c1} increments fit to the data”, was changed to “(f) The corresponding fits to the data at different f_{c1} increments”. In section 3.2, “ f_{c2} ” was changed to “ f_{c2} ”. In section 4.2, “ 5×10^{13} N m do show no visible dependency on magnitude”, was changed to “ 5×10^{13} N m show no visible dependency on magnitude”.